

Spatially-resolved spectroscopic study of arcjet helium plasmas expanding through a rectangular-shaped converging-diverging nozzle

Shinichi NAMBA^{*}, Noriyasu YASHIO, Kazuki KOZUE, Keisuke NAKAMURA, Takuma ENDO, Ken TAKIYAMA

Graduate School of Engineering, Hiroshima University, 1-4-1 Kagamiyama, Higashi-Hiroshima, Hiroshima 739-8527 JAPAN

Kuninori SATO

National Institute for Fusion Science, 322-6 Oroshi-cyo, Toki, Gifu 509-5292 JAPAN

(Received)

KEYWORDS: arcjet plasma, plasma spectroscopy, atomic and molecular physics, recombination plasma

PACS number: 52.25.Os, 52.70.Kz, 52.77.Fv, 52.80.Mg

An arcjet discharge device with a rectangular-shaped converging and diverging nozzle has been developed, which allowed us to optically observe high density plasmas inside the anode nozzle. Spectroscopic observation along the plasma expansion axis was carried out to examine the characteristics of the arc plasma inside the nozzle. Analyzing the intense continuum and line emission spectra, we successfully obtained the spatial variations of electron temperature and density. Moreover, it was found that two dimensional optical measurement was of great use in visualizing the transition from the atmospheric thermal plasma to strongly non-equilibrium recombining phase due to an adiabatic expansion.

^{*}E-mail address: namba@hiroshima-u.ac.jp

1. Introduction

Atmospheric thermal plasmas have been extensively studied for applications in various engineering and scientific fields [1]. One of the thermal plasmas, an arc plasma expanding through a converging and diverging nozzle with Laval or conical shape is expected as a compact electrothermal engine and thruster [2]. According to the theory of compressible flow dynamics, an enthalpy of hot gas is converted into the directional kinetic energy due to an adiabatic free expansion into vacuum [3], and thus the electric propulsion with a high specific impulse can be realized. Arcjet thrusters with the power range from a few hundreds W to 100-kW class have been developed for the main engine system of a spacecraft and the orbital and attitude control of a small satellite so far [4].

In addition, the arcjet plasma operated with reactive gases has also attracted a great deal of interest in chemical vapor deposition (CVD) [5]. For example, hydrocarbon/hydrogen/argon arc plasma could provide an ideal environment for synthesis of diamond film with high quality [6]. Since the diamond growth rate on the substrate is given by a complicated function of plasma parameters, such as plasma density, temperature and gas pressure, much effort has been devoted to establish an optimal condition for the efficient deposition.

On the other hand, a stationary plasma generated with a direct current (DC) modified arc discharge has served as a powerful source for the research of atomic and molecular processes. In particular, rapid plasma cooling due to collision of high density plasma with the ambient gas can create a non equilibrium recombining plasma and provide a favorable condition for population inversions. In fact, a formation of stationary inverted population between $n=2$ and 5 levels of He^+ ion, which is capable of generating a lasing action for a continuous vacuum ultraviolet (VUV) laser, was demonstrated in TPD device [7, 8]. In addition, Akatsuka *et al.* demonstrated that for hydrogen plasmas the large population inversion relevant to $n=3-4$ transition was produced in the magnetically trapped expanding arcjet plasma [9, 10]. Meanwhile, the plasma with the high enthalpy flow generated by arc type discharge has been used for fundamental research of a magnetically confined fusion plasma, e.g., the study of recombination process occurring in the divertor/edge region [11, 12], where the plasma facing component will be exposed to the significantly high heat flux diffusing from the core region [13, 14].

Recently, we developed the compact DC arcjet plasma source for fundamental studies on arcjet thrusters and atomic and molecular physics in plasmas [15]. The high density He plasmas expanding through the converging-diverging conical nozzle were observed with a visible spectrometer. The analysis of continuum and line emissions from Rydberg states showed that the expanding plasma had the electron temperature of 0.3 eV and density of $2 \times 10^{15} \text{ cm}^{-3}$ at the position of 45 mm from the nozzle exit. Moreover, the dynamics of the plasma expanding from the anode nozzle was investigated by a shadowgraph method, indicating that the thermal pinch effect came into play. However, the direct measurements of the interior of the anode nozzle could not be accomplished. Although the line-of-sight observation from the end viewport was also performed to deduce the plasma parameters inside the nozzle, the spectroscopic analysis yielded only the averaged plasma density and temperature over the expansion axis.

The direct observation of the arc discharge section is essential to understand the ionization and recombination processes and expansion dynamics. In fact, the two dimensional (2D) low power DC arcjet apparatus was developed to investigate the discharge behavior and its relation with thrust performance on the electric propulsion system [16]. It was found that two different discharge modes, that is, high voltage stabilized mode and low voltage unstable mode, occurred and this transition was closely correlated with the arc discharge channel around the nozzle throat (constrictor). On the other hand, the process of the electrode deteriorations due to melting, erosion and evaporation of the material should be clarified for a reliable long time operation of the arc discharge. Moreover, the transport of impurity originating from the electrode material is also important subject to improve the quality of CVD films.

In this study, an arc discharge device with a rectangular-shaped anode nozzle has been developed, so that we can observe the 2D emission profile of thermal arc plasmas generated inside the nozzle. In order to examine the characteristics of arcjet He plasmas, first, spectroscopic observations along the expansion axis were conducted with a visible spectrometer. From analysis of continuum and line emission, we successfully obtained the spatial variations of electron density and temperature. On the other hand, 2D emission measurements using optical bandpass filters were also performed to visualize the phase transition from the atmospheric thermal plasma to non-equilibrium recombining plasma.

2. Experimental Setup

2.1. Arcjet discharge device with the rectangular nozzle

Figures 1(a) and (b) show a photograph and schematic diagram of the expanding arcjet generator, respectively, which has been developed to directly observe the thermal arc plasma generated in the nozzle. A pair of molybdenum (Mo) anode was installed in the discharge assembly with a separation of 0.5 mm, which served as a converging-diverging slit type nozzle for the jet expansion. The throat width and length were 10.0 and 1.0 mm, respectively, and the diverging angle was 30°. Quartz windows were employed as the side walls to constrict the lateral gas expansion.

The high density He arc plasmas were generated between the anode and a needle-shaped cathode (cerium tungsten (Ce/W) rod). The gap length between the anode and cathode was set to be 1.0 mm, and the discharge current and voltage were up to 50 A and ~20 V, respectively. The gas pressure at the discharge section was around 90 kPa. With the help of large pumping system to evacuate the residual gas, the pressure in the expansion chamber was kept to be less than 5 kPa. This enables the arc plasma to undergo the adiabatic expansion, resulting in the production of high density and low temperature recombining plasma in the downstream from the nozzle throat [8].

2.2. Spectroscopic observation

In order to characterize the arcjet plasmas and investigate the expansion dynamics, first, the spatially-resolved emission spectra along the expansion axis were measured by using a 0.5-m visible spectrometer (gratings: 150 or 1200 grooves/mm). The detector was a charged coupled device (CCD)

camera with an image intensifier. The plasma was imaged by a quartz lens onto an end of optical bundled fiber with 48 cores. The transmitted light through the fiber was imaged by a lens again onto an entrance slit of the spectrometer. Spectral range observed using this system was $\lambda=250\text{-}750$ nm. Figure 2 shows a schematic diagram of the spectroscopic observation. When the emission above 400 nm was measured, a sharp cut filter was used to block the second and third order spectra. Spectral sensitivity of the whole optical system was calibrated by standard lamps (tungsten ribbon and xenon discharge lamps). The resolution of the optical system was determined by measuring a He-Ne laser spectrum ($\lambda=632$ nm). Given that the instrumental function can be expressed by a Gaussian shape, we obtained the width of 58 pm (full width at half maximum: FWHM) for the grating of 1200 grooves/mm and slit width of 10 μm .

On the other hand, 2D images at selected wavelengths were observed with optical bandpass filter and a CCD camera. The spatial resolution was around 23 μm . As described later, the continuum radiation as well as He line spectra was emitted from the arc plasma. To distinguish these components, the bandpass filters having the design wavelengths of $\lambda=615$ and 587 nm (bandwidth: ~ 2 nm) were used for the measurements of continuum and He atomic spectrum, respectively.

3. Results and Discussion

3.1. Continuum radiation and determination of plasma temperature

Figure 3 shows the UV and visible spectra observed at the position of $x=3$ mm. Here the position x is defined as the distance from the cathode, as shown in FIG. 1(a) and FIG. 2. The discharge current was 50 A, and the low dispersion grating with 150 grooves/mm was used. As clearly seen, the intense line spectra that can be assigned to He atomic emissions were observed, while continuum radiation was also emitted and the intensity significantly increased with decreasing photon energy. For relatively dense plasmas, the expected origins of continuum emission concern the bremsstrahlung and radiative recombination [17, 18]. Note that for optically-thick limit the bremsstrahlung emission can be described by the Planck radiation law (see below).

The spectral intensity $I(\nu, z)$ at the frequency ν and the position z is given by solving the equation of radiative transfer [18]:

$$\frac{dI(\nu, z)}{dx} = \varepsilon(\nu, z) - \kappa'(\nu)I(\nu, z), \quad (1)$$

where $\varepsilon(\nu, z)$ and $\kappa'(\nu, z)$ are the emission and absorption coefficients, respectively. If we consider that the plasma extends between $z=0$ and $z=z_0$, the solution with the boundary condition of $z=0$, $I(\nu, 0)=I_0(\nu)$, is given by,

$$I(\nu, z_0) = I_0(\nu) \exp\left(-\int_0^{z_0} \kappa'(\nu, z) dz\right) + \int_0^{z_0} \left[\varepsilon(\nu, z) \exp\left(-\int_z^{z_0} \kappa'(\nu, z) dz\right) \right] dz. \quad (2)$$

For a homogeneous plasma, we obtain the following equation:

$$I(\nu, z_0) = \frac{\varepsilon(\nu)}{\kappa'(\nu)} (1 - \exp(-\kappa'(\nu)z_0)). \quad (3)$$

On the other hand, if the bremsstrahlung dominates the continuum radiation, the emission coefficient follows from Kramers' calculation as [17]:

$$\varepsilon(\nu) = \frac{n_e}{4\pi} \frac{2^7}{(6\pi)^{3/2}} \left(\frac{m_e}{k_B T_e}\right)^{1/2} \frac{e^6}{c^3 m_e^2} \exp\left(-\frac{h\nu}{k_B T_e}\right) \sum_Z n_Z Z^2 g_{\text{ff}}^Z, \quad (4)$$

where n_e is the electron density and T_e is the electron temperature, k_B is the Boltzmann constant, m_e is the mass of electron, Z is the charge number, n_Z is the density of Z^+ ion, g_{ff}^Z is the Gaunt factor for free-free transition and the other notations have the usual meanings. For thermal equilibrium plasma, the absorption coefficient is also calculated by using Kirchhoff's law:

$$\kappa'(\nu) = \frac{n_e}{4\pi} \frac{2^6}{(6\pi)^{3/2}} \left(\frac{m_e}{k_B T_e}\right)^{1/2} \frac{e^6}{h c m_e^2 \nu^3} \left[1 - \exp\left(-\frac{h\nu}{k_B T_e}\right)\right] \sum_Z n_Z Z^2 g_{\text{ff}}^Z. \quad (5)$$

Here, Kirchhoff's law expressing the relation between the emission and absorption coefficients is given by (T_R : radiation temperature):

$$\frac{\varepsilon(\nu)}{\kappa'(\nu)} = \frac{2h\nu^3}{c^2} \frac{1}{\exp(h\nu/k_B T_R) - 1}. \quad (6)$$

By substituting Eqs. (5) and (6) into Eq. (3), we can derive the continuum light emitted from the plasma surface. **Figure 4 shows the density dependence of the spectral distribution for a plasma with the temperature of 10,000 K (typical value for arc discharge) and plasma length of 10 mm. As clearly seen, in the case of density of $1 \times 10^{18} \text{ cm}^{-3}$ and at low frequencies the plasma radiates the spectrum like a black body having a radiation temperature equivalent to the kinetic temperature of the electrons. While at high frequencies the black body spectrum gives way to the bremsstrahlung radiation, because the absorption coefficient becomes small at high photon energy. For the plasma density of $1 \times 10^{16} \text{ cm}^{-3}$, which is typical value for the atmospheric arc plasmas, the absorption coefficient at $h\nu = 2.5 \text{ eV}$ ($\lambda \sim 0.5 \text{ }\mu\text{m}$) is as small as $\kappa' = 1.6 \times 10^{-6}$. It is, therefore, reasonable to suppose that the plasma is optically thin and Eq. (4) describing the emission coefficient holds for**

optical frequencies. In order to determine the temperature, the experimental data is fitted with Eq. (4), as shown in FIG. 3. For $x=3.0$ mm and 50 A, the temperature of ~ 0.18 eV is obtained.

On the other hand, another continuum which is superposed on the bremsstrahlung radiation seems to appear in the UV region, as shown in FIG. 4. The UV continuum around 3.6 eV can be interpreted in terms of the radiative recombination terminated to $2p\ ^3P$ transition, that is, $\text{He}^+ + e \rightarrow \text{He}^* (2p\ ^3P) + h\nu$ [8,15,19]. Note that the series limit for an isolated atom shifts to the lower energy side due to the lowering of ionization potential [18]. The emission coefficient $\varepsilon(\nu)$ relevant to this free-bound transition is given by the following equation [18,19],

$$\varepsilon(\nu) = \frac{h^7}{8\pi^{9/2}m_e^3e^6} \frac{\nu^3}{c^2} \frac{g}{g_z} \sigma n_e n_z \left(\frac{E_H}{k_B T_e} \right)^{3/2} \exp \left[\frac{1}{k_B T_e} (\chi - h\nu) \right], \quad (7)$$

where g and g_z are the statistical weights of the ground state of atom and He^+ ion, respectively, σ is the photo-ionization cross section for the ground state of He atom [19], E_H is the ionization energy of H atom, and χ is the ionization energy from He atom ground state. In a similar manner to the bremsstrahlung radiation, the electron temperature can be obtained from the tangent of the straight line of $\log(\varepsilon(\nu)/(\nu^3\sigma(\nu)))$ plot on the photon energy. Figure 5 represents the experimental data observed with the grating of 1200 grooves/mm and the best fitted curve corresponding to $T_e=0.15$ eV.

The spatial variations of the temperature drawn from both methods are plotted in FIG. 6. No distinct emission associated with the radiative recombination was observed at $x=0$ mm. A good agreement between both temperatures has been obtained, apart from the value at $x=4$ mm. It is highly probable that since the line emission at $x=4$ mm was very intense compared with the continuum light and broadened due to the Stark effect (see later), the temperature evaluated by the bremsstrahlung might be overestimated. On the other hand, the temperature at $x=0$ mm, $T_e \sim 0.28$ eV, was not high enough to generate the thermal arc plasma (ionization potential of He atom: 24.6 eV), indicating that this method of temperature determination was not applicable to the cathode region. The reason for the underestimation of the temperature at $x=0$ mm could be found in the intense radiation from the cathode itself, from which the thermal electrons were emitted. Note that the surface temperature of the cathode is around 2,000 K, so that the significant fraction of the radiation in visible and IR regions was emitted from the cathode. **In fact, the thermal radiation from the cathode surface ($x=0$ mm) was by ten times stronger than the plasma continua at $x=1$ mm (bremsstrahlung and radiative recombination).** Hence, the contribution of the cathode radiation had to be also taken into account for $x=0$ mm.

Assuming that the plasma expanding through the slit nozzle was described by the idealized continuum flow (adiabatic and isentropic expansion), we can estimate the plasma temperature, T_0 , at $x=0$ mm (source temperature). According to the hydrodynamic theory, the Mach number, M , for the slit nozzle at the throat downstream, X , is given by [20],

$$M(X) = A_S \left(\frac{X - X_0}{D} \right)^{(\gamma-1)/2} - B_S \left(\frac{X - X_0}{D} \right)^{-(\gamma-1)/2}, \quad (9)$$

where D is the slit height, A_S , B_S , X_0/D are parameters depending on the ratio of heat capacities, γ , ($\gamma=5/3$ for He). In addition, the temperature is given by the following equation.

$$\frac{T(X)}{T_0} = \left[1 + \frac{\gamma-1}{2} M(X)^2 \right]^{-1}, \quad (10)$$

The theoretical curve in such a way that the temperature at the throat downstream was reproduced by the expected curve is shown in FIG. 6 (source temperature: 1.3 eV). The temperature of 1.3 eV yields the ionization degree of 1×10^{-3} under the Saha equilibrium condition, resulting in the generation of atmospheric thermal plasmas.

3.2. Stark broadening and determination of electron density

In order to determine the electron density, the atomic emission (667.8 nm, transition: $2p \ ^1P-3d \ ^1D$) was measured with the grating of 1200 grooves/mm. Figure 7 shows the spectral profiles at different spatial positions. The spectrum at $x=0.5$ mm was obviously broadened, whereas with moving away from the cathode the line profile became narrower. In general, the spectrum observed can be expressed by the Voigt function, which is a convolution of a Gaussian (Doppler and instrumental width) and Lorentzian (resonance and Stark broadenings) line shapes. In the present study, however, the gas temperature was so high that the resonance broadening could be neglected [21]. Moreover, assuming that Gaussian profile is given by only the instrumental function ($\Delta\lambda_I = 58$ pm), the Lorentzian width of 667.8 nm emission at $x=0.5$ mm was determined to be $\Delta\lambda_S \sim 45.7$ pm (FWHM) by deconvolution procedure.

Meanwhile, the Stark FWHM $\Delta\lambda_S$ of atomic line (in Å) is approximately given by the following equation over a wide range of electron densities (cm^{-3}) and temperatures (K) [17].

$$\Delta\lambda_S \sim 2\omega \left[1 + 1.75 \times 10^{-4} n_e^{1/4} \alpha \left(1 - 0.068 n_e^{1/6} T_e^{-1/2} \right) \right] \times 10^{-16} n_e \quad (11)$$

Here, ω is the half width at half maximum (HWHM) due to electron impacts and α is the ion broadening parameter. Since these variables depend on the temperature, we inferred them for various temperatures by using the values listed in Ref. 22. By substituting the temperature derived from the above and the Stark width into Eq. (11), the electron density was determined to be $4.0 \times 10^{15} \text{ cm}^{-3}$ for $x=0.5$ mm. The spatial variation of the electron density under the current of 50 A is plotted in FIG. 8. For $x=0$ mm, the density was probably underestimated, because the temperatures determined by continuum spectra were invalid at the cathode, as described above. According to the Saha equation,

the ionization degrees corresponding to $T_e=0.15, 0.3, 0.5$ eV are calculated to be $1 \times 10^{-35}, 7 \times 10^{-18}, 5 \times 10^{-10}$, respectively, and thus the plasma densities under the thermal equilibrium are far from those determined from the Stark width. The strongly non-equilibrium plasmas, therefore, were generated due to the rapid plasma cooling.

For the ideal flow expanding through the slit nozzle, **which was described in Sec. 3.1**, the density decreases as X^{-1} for short distance from the throat [20] and thus the linear fit for the electron density was made to elucidate the validity of this assumption, as shown in FIG.8. The density derived from the Stark width decreased linearly for $x \geq 1.0$ mm ($X \geq 0$ mm), so that we could apply the idealized continuum flow model to the arcjet plasmas generated in this study.

3.3. 2D images of expanding arcjet plasmas

Figure 9 shows the 2D monochromatic images of the He arcjet plasmas (615 or 587 nm) under the discharge current of 50 A. No line emission appeared in 615nm (see FIG. 4), so that the 2D images observed using 615-nm filter represent the spatial distribution of the continuum radiation. As seen, the most intense emission was obtained at the cathode (FIG. 9(b), (d)). With increasing distance from the cathode, the intensity of 615 nm decreased drastically towards the nozzle exit (c), indicating that the bremsstrahlung ceased due to the plasma expansion. In contrast, for 587 nm the bright emission was also observed around the nozzle throat, as shown in (e). Note that the line intensity is expressed as a function of electron temperature and plasma and neutral densities. Moreover, for high density plasmas the radiation trapping relevant to resonance lines significantly affects the population kinetics. In order to clarify the origin of the second emission peak at $x=2$ mm, therefore, the analysis by using the collisional-radiative model for He atom [23, 24] was performed. Here, we assume the optically thick plasma with gas (heavy particle) temperature of 1,000 K and its density of 2×10^{19} cm⁻³. By employing the plasma temperature and density derived above, the population of 3^3D that is the upper level of 587 nm transition was calculated. As shown in FIG. 10, the population reaches maximum value at $x=2$ mm. Considering that the line intensity is in proportion to the 3^3D population, the numerical calculation appears to match the trend in the spatial emission behavior observed.

In order to elucidate the mechanism underlying the bright emission observed near $x=2$ mm, we calculated the collisional-radiative recombination coefficient that is a measure of how fast the plasma would be neutralized into atoms. As seen in FIG. 10, the coefficient also has the highest value at $x=2\sim 3$ mm, implying that the thermal plasma turned into the strongly non-equilibrium recombining plasma around there due to the adiabatic expansion. For relatively high density plasmas ($\geq 10^{13}$ cm⁻³), the volumetric recombination dominates and thus follows the collisional-radiative cascade into 3^3D level. Hence, the mechanism responsible for the second emission peak observed could be ascribed to the plasma recombination followed by the cascade processes into the excited states. Therefore, the 2D imaging has the potentials to provide not only the information on where the strong plasma recombination could occur but also a simple method to

visualize the transition of the thermal arc plasma into non-equilibrium recombining plasma.

4. Summary

In order to optically diagnose the He arcjet plasmas inside the nozzle, we have developed the arc plasma discharge device having the rectangular-shaped anode nozzle.

Spectroscopic observations along the expansion axis were carried out to determine the electron temperature and density. Intense continuum emission arising from the bremsstrahlung was observed. Comparison of the experimental spectra with the theoretical bremsstrahlung curve yielded the temperature of ~ 0.18 eV at the position of $x=3.0$ mm from the cathode and the current of 50 A. Moreover, in UV region another continuum spectra associated with the radiative recombination process also appeared. This recombination continuum showed that the thermal arc plasma could undergo the rapid cooling due to the adiabatic expansion. The temperature of ~ 0.15 eV was also determined by the recombination continuum, which was in good agreement with that derived from the bremsstrahlung. As for the determination of electron density, we measured the Stark broadening spectrum relevant to He atom (667.8 nm). The density evaluated from the line width was as high as $4.0 \times 10^{15} \text{ cm}^{-3}$ for $x=0.5$ mm and 50 A.

We measured the 2D monochromatic images of the continuum and atomic emission to examine the behavior of the plasma expansion. The continuum light decreased monotonically along the expansion axis, whereas the atomic emission had the double emission peaks ($x=0$ and 2 mm). The numerical calculation using the collisional-radiative model demonstrated that the bright emission observed at the throat ($x=2$ mm) was closely related to the production of non-equilibrium plasma in the strong recombination phase. As a result, the 2D emission images could provide a simple method for visualization of the transition of the atmospheric thermal arc plasma into recombining plasma.

Acknowledgements

We would like to thank Prof. H. Akatsuka (Tokyo Institute of Technology) and Prof. K. Ono (Kyoto University) for helpful discussions to construct and design the arcjet plasma generator. This work was performed with the support and under the auspices of the NIFS Collaborative Research Program (NIFS08KQHH015).

References

- [1] M. I. Boulos, P. Fauchais and E. Pfender, *Thermal Plasmas: Fundamentals and Applications* (Plenum, 1994).
- [2] E. Choueiri ed., *Physics of Plasma Propulsion* (CRC press, 2007).
- [3] J. D. Anderson, Jr., *Modern Compressible Flow with Historical Perspective*, 2nd ed. (McGraw Hill, New York, 1989).
- [4] For example, G. P. Sutton, *Rocket Propulsion Elements: Introduction to the Engineering of Rockets* (John Wiley & Sons, 1992)
- [5] D.M. Dobkin and M.K. Zuraw, *Principles of Chemical Vapor Deposition* (Kluwer Academic, 2003).
- [6] M. A. Cappelli and T. G. Owano, *Low-Pressure Synthetic Diamond*, edited by B. Dischler, C.Wild (Springer 1998).
- [7] K. Sato, M. Shiho, M. Hosokawa, H. Sugawara, T. Oda and T.Sasaki, *Phys.Rev.Lett.***39**, 1074 (1977).
- [8] S. Namba, M. Goto, H. Tsuboi, T. Oda, K. Sato, *J. Appl. Phys.* **88**, 3182 (2000).
- [9] H. Akatsuka and M. Suzuki, *Phys. Rev. E*, **49**, 1534 (1994).
- [10] H. Akatsuka and M. Suzuki, *Contrib. Plasma Phys.*, **34**, 539 (1994).
- [11] T. W. Petrie, R. Maingi, S. L. Allen, D. A. Buchenauer, D. N. Hill and C. J. Lasnier, *Nucl. Fusion*, **37**, 643 (1997).
- [12] S. Kado, Y. Iida, S. Kajita, D. Yamasaki, A. Okamoto, B. Xiao, T. Shikama, T. Oishi and S. Tanaka, *J. Plasma Fusion Res.*, **81**, 810 (2005).
- [13] R. Parker, G. Janeschitz, H. D. Pacher, D. Post, S. Chiochio, G. Federici, P. Ladd, and ITER, Joint Central Team, Home Teams, *J. Nucl. Mater.* **241–243**, 1 (1997).
- [14] G. Janeschitz, K. Borrass, C. Federici, Y. Igitkhanov, A. Kukushukin, H. D. Pacher, G. W. Pacher, and M. Sugihara, *J. Nucl. Mater.* **220–222**, 73 (1995).
- [15] S. Namba, K. Nakamura, N. Yashio, S. Furukawa, K. Takiyama and K. Sato, *J. Plasma and Fusion Res. SERIES* (in press).
- [16] K. Ogiwara, S. Hosoda, I. Kimura, H. Kuninaka, K. Toki and K. Kuriki, *J. Japan Soc. Aero. and Space Science*, **48**, 250 (2000) [in Japanese].
- [17] W. L. Wiese, *Plasma Diagnostic Techniques*, edited by R. H. Huddlestone and S. L. Leonard (Academic, New York, 1965).
- [18] J. Richter, *Plasma Diagnostics*, edited by W. Lochte-Holtgreven, (Elsevier Science, 1968).
- [19] M. Otsuka, R. Ikee, and K. Ishii, *J. Quant. Spectrosc. Radiat. Transf.* **15**, 995 (1975).
- [20] M. D. Morse, “Supersonic Beam Sources”, in *Atomic, Molecular, and Optical Physics: Atoms and Molecules*, Vol. 29B, edited by F. B. Dunning and R. G. Hulet (Academic, San Diego, 1996).
- [21] H. R. Griem, *Spectral Line Broadening by Plasmas* (Academic, New York, 1974).
- [22] H. R. Griem, *Plasma Spectroscopy* (McGraw Hill, New York, 1964).
- [23] T. Fujimoto, *J. Quant. Spectrosc. Radiant. Transf.* **21**, 439 (1979).
- [24] M. Goto and T. Fujimoto, *NIFS Data* **43** (National Institute for Fusion Science, Gifu, Japan, 1997).

Figure Captions

Figure 1, Photograph (a) and schematic (b) of the arcjet plasma device. Helium plasma expands through the rectangular-shaped converging-diverging anode nozzle that enabled us to directly observe the plasma generated inside the nozzle.

Figure 2, Schematic view of the spectroscopic observation along the expansion axis.

Figure 3, UV and visible spectra emitted from the arcjet He plasma. The optical measurement was carried out at the position of $x=3$ mm from the cathode under the discharge current of 50 A and gas pressure of 90 kPa. Assuming that the bremsstrahlung dominated the continuum radiation, we derived the electron temperature T_e from Eq. (4). In the figure, the straight line corresponds to the electron temperature of 0.18 eV.

Figure 4, Spectral distributions calculated by using Eq. (3) for a plasma with the temperature of 10,000 K and plasma length of 10 mm. Planck distribution curve is also shown for comparison. For plasma density of $1 \times 10^{20} \text{ cm}^{-3}$ the continuum spectrum at $\nu \leq 2 \times 10^{15} \text{ s}^{-1}$ can be well expressed by the black body radiation.

Figure 5, The radiative recombination continuum ($\text{He}^+ + e \rightarrow \text{He}^* (2p^3P) + h\nu$) and line emission relevant to high Rydberg states ($nd^3D \rightarrow 2p^3P$ transition). By scaling the vertical axis as $\epsilon(\nu)/(\nu^3\sigma)$, the electron temperature can be determine by the tangent of the straight line of semi-log plot. The temperature under the condition of FIG. 3 was as low as 0.15 eV.

Figure 6, Spatial variations of the electron temperature obtained by analyzing the bremsstrahlung and radiative recombination spectra (50A). The solid line represents the theoretical curve corresponding to the source temperature of 1.3 eV.

Figure 7, Atomic spectra of He 667.8 nm (transition: $2p^1P-3d^1D$). The line spectra observed adjacent to the cathode were broadened due to the Stark effect.

Figure 8, Spatial variation of the electron density at the discharge current of 50 A. We calculated the density from the Stark broadening width of He 667.8 nm, which is drawn from the deconvolution procedure of the experimental curve with a Voigt profile. For $x \geq 1.0$ mm, the density decreased linearly, as expected by the continuum flow model.

Figure 9, 2D monochromatic emission images of plasma expansion taken by using the optical bandpass filters, 615 nm for (b) and (c), 587 nm for (d) and (e). As for (b) and (d), the thick ND filters were used for the appropriate light reduction.

Figure 10, Population of $3d\ ^3D$ level and the collisional-radiative recombination coefficient were calculated using the He collisional-radiative model.

Figure 1, S. Namba et al., JJAP

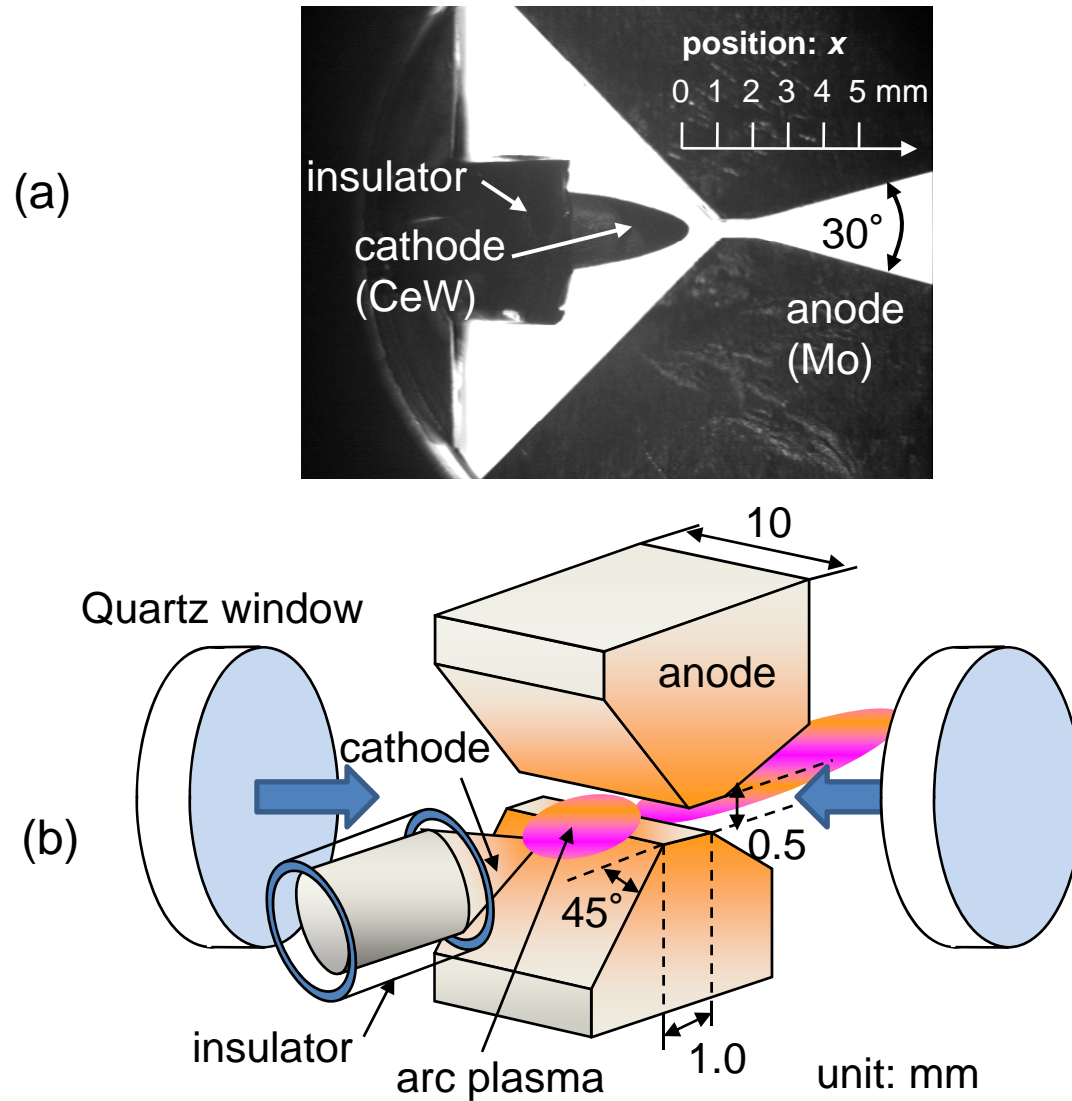


FIG.1.,

Photograph (a) and schematic (b) of the arcjet plasma device. Helium plasma expands through the rectangular-shaped converging-diverging anode nozzle that enables us to directly observe the plasma generated inside the nozzle.

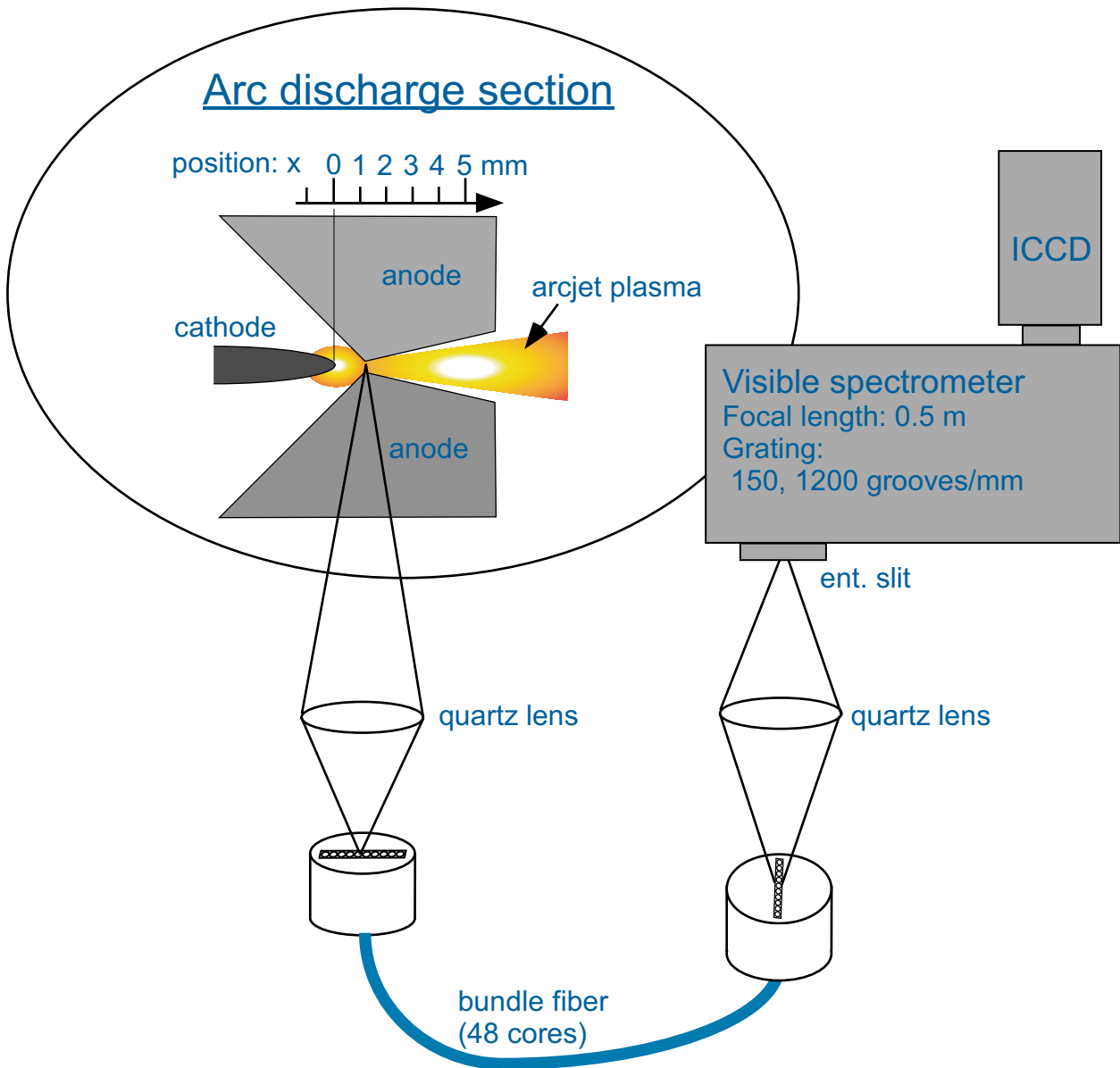


Figure 2., Schematic view of the spectroscopic observation along the expansion axis.

Figure 3, S. Namba et al., JJAP

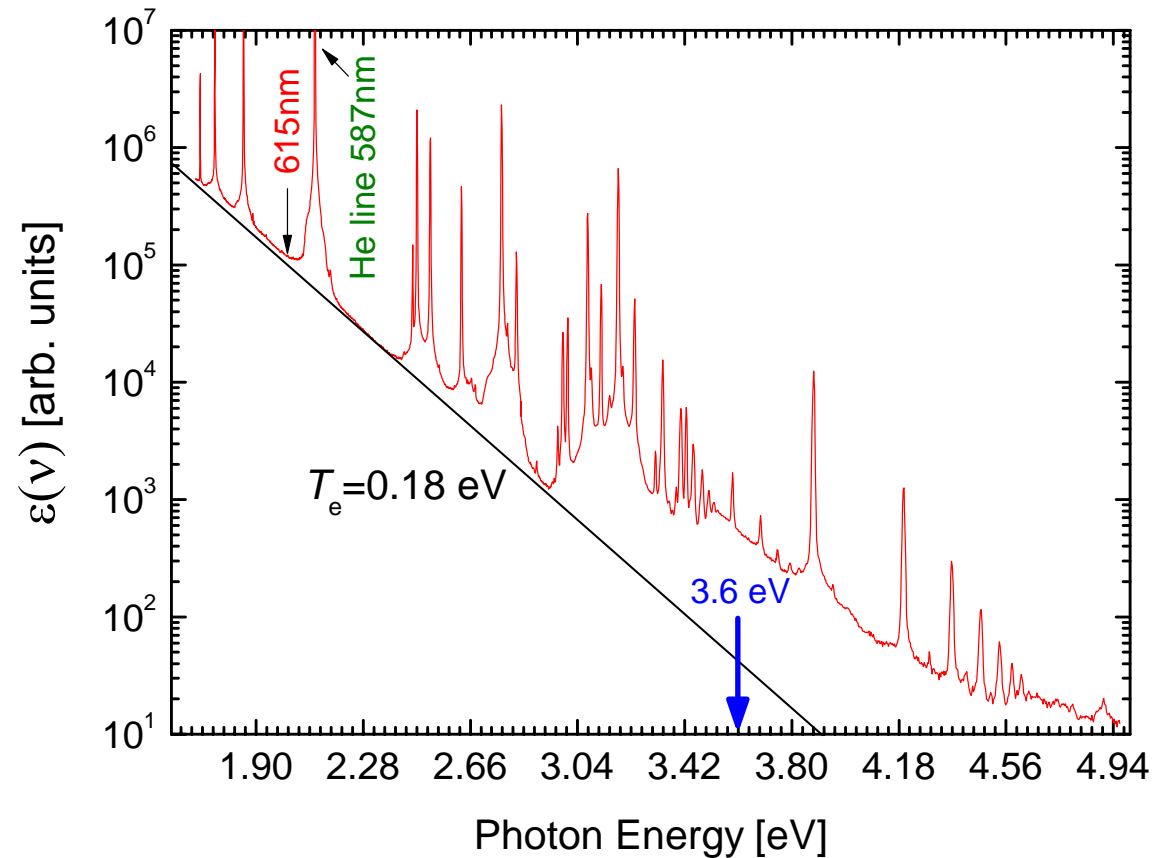


Figure3. ,

UV and visible spectra emitted from the arcjet He plasma. The optical measurement was carried out at the position of $x=3$ mm from the cathode under the discharge current of 50 A and gas pressure of 90 kPa. Assuming that the bremsstrahlung dominated the continuum radiation, we derived the electron temperature T_e from Eq. (4). In the figure, the straight line corresponds to $T_e=0.18$ eV.

Figure 4, S. Namba et al., JJAP

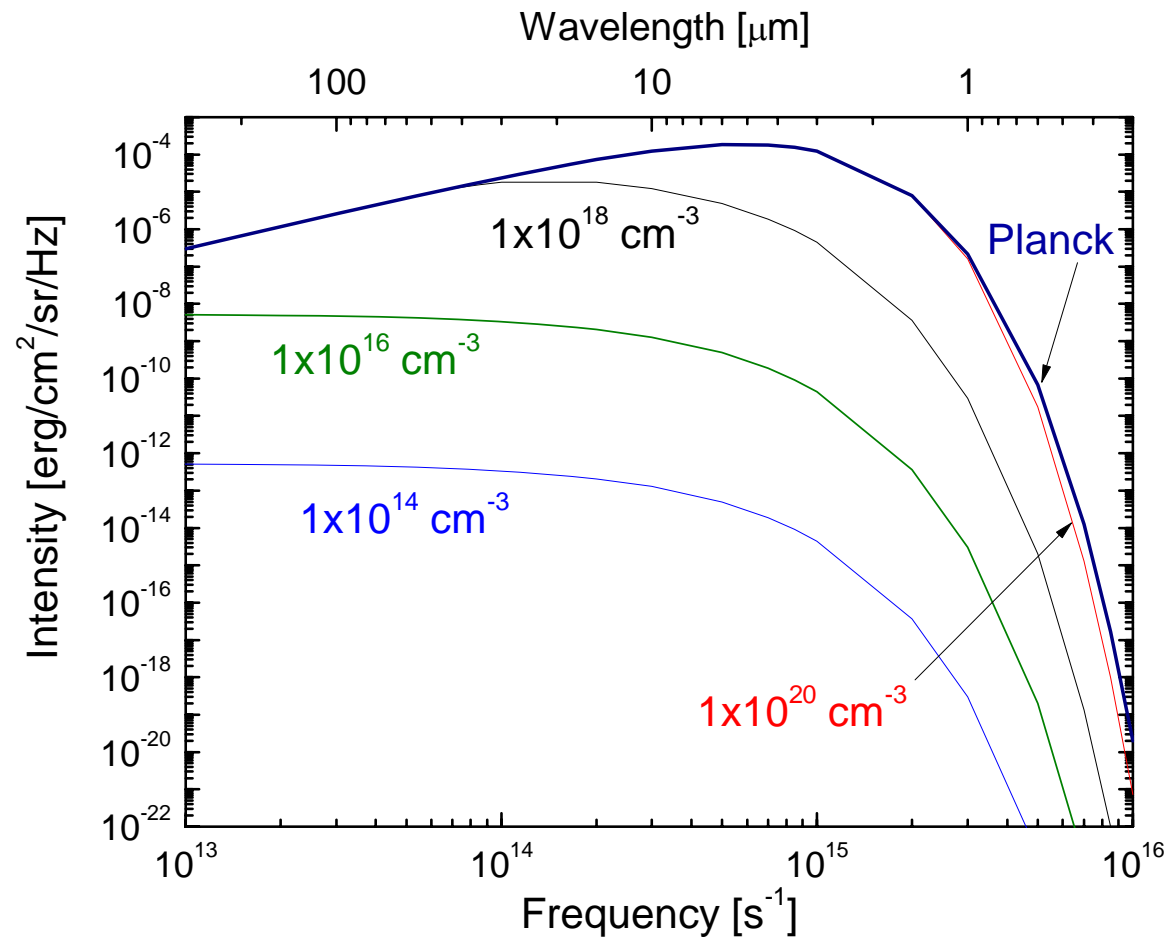


Figure 4.,
Spectral distributions calculated by using Eq. (3) under a temperature of 10,000 K and plasma length of 10 mm. Planck distribution curve is also shown for comparison. For plasma density of $1 \times 10^{20} \text{ cm}^{-3}$ the continuum spectrum at $\nu \leq 2 \times 10^{15} \text{ s}^{-1}$ can be well expressed by the black body radiation.

Figure 5, S. Namba et al., JJAP

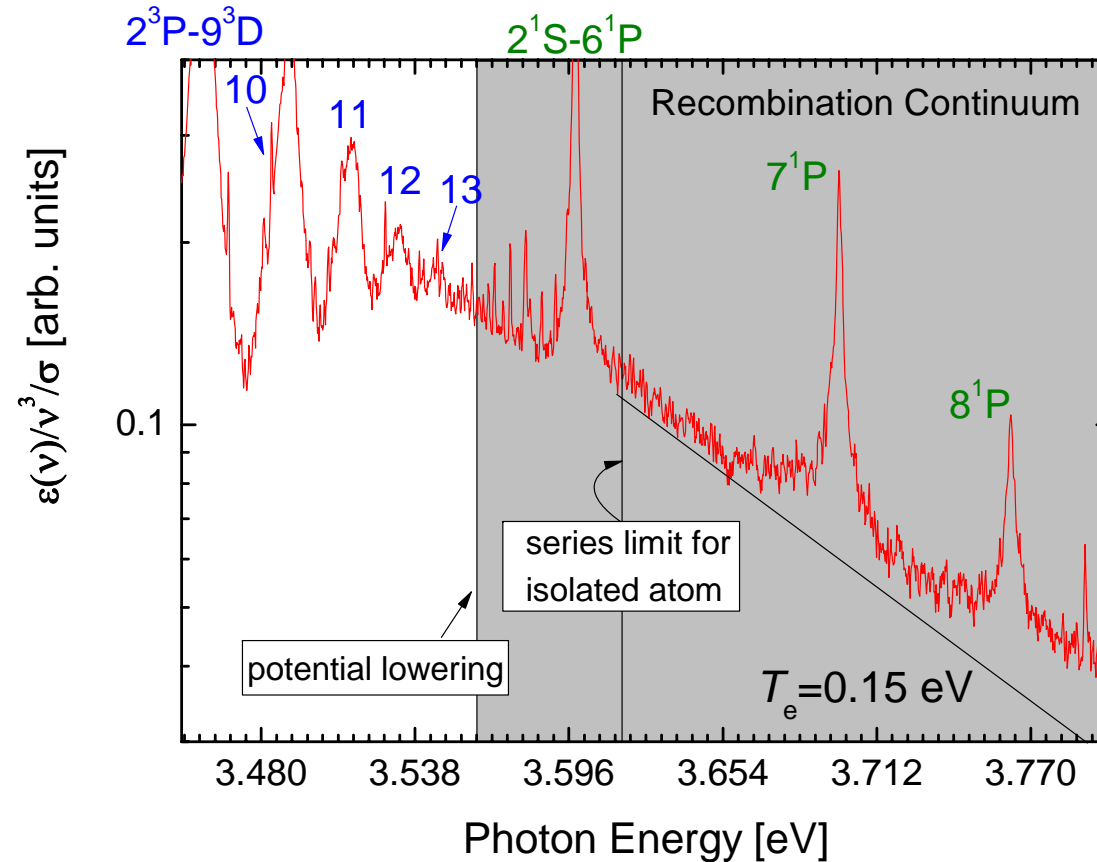


Figure 5.,

The radiative recombination continuum ($\text{He}^+ + e \rightarrow \text{He}^* (2p \ ^3P) + h\nu$) and line emission relevant to high Rydberg states ($nd \ ^3D \rightarrow 2p \ ^3P$ transition). By scaling the vertical axis as $\log(\varepsilon(\nu)/\nu^3/\sigma)$, the electron temperature can be determined by the tangent of the straight line of semi-log plot. The temperature under the condition of FIG. 3 was as low as 0.15 eV.

Figure 6, S. Namba et al., JJAP

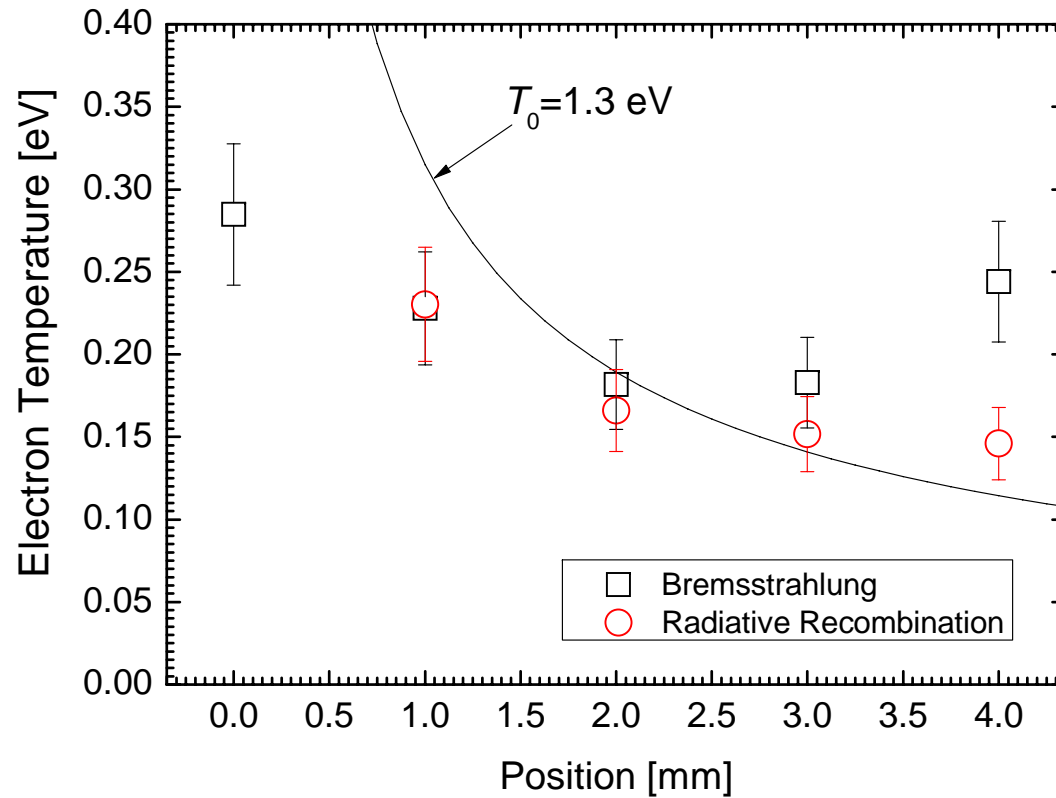


Figure 6.,
Spatial variations of the electron temperature obtained by analyzing the bremsstrahlung and radiative recombination spectra (50A). The solid line represents the theoretical curve corresponding to the source temperature of 1.3 eV.

Figure 7, S. Namba et al., JJAP

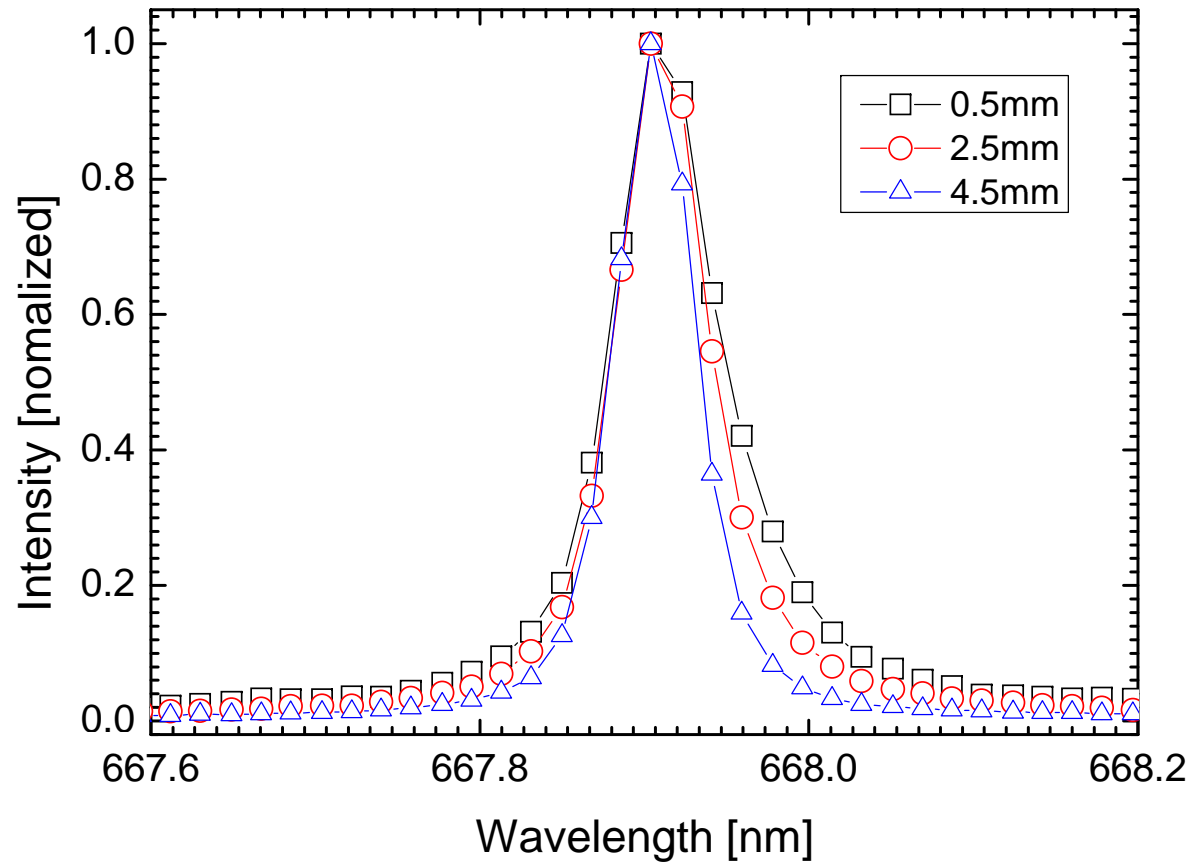


Figure 7.,
Atomic spectra of He 667.8 nm (transition: $2p^1P-3d^1D$). The line spectra observed adjacent to the cathode were broadened due to the Stark effect.

Figure 8, S. Namba et al., JJAP

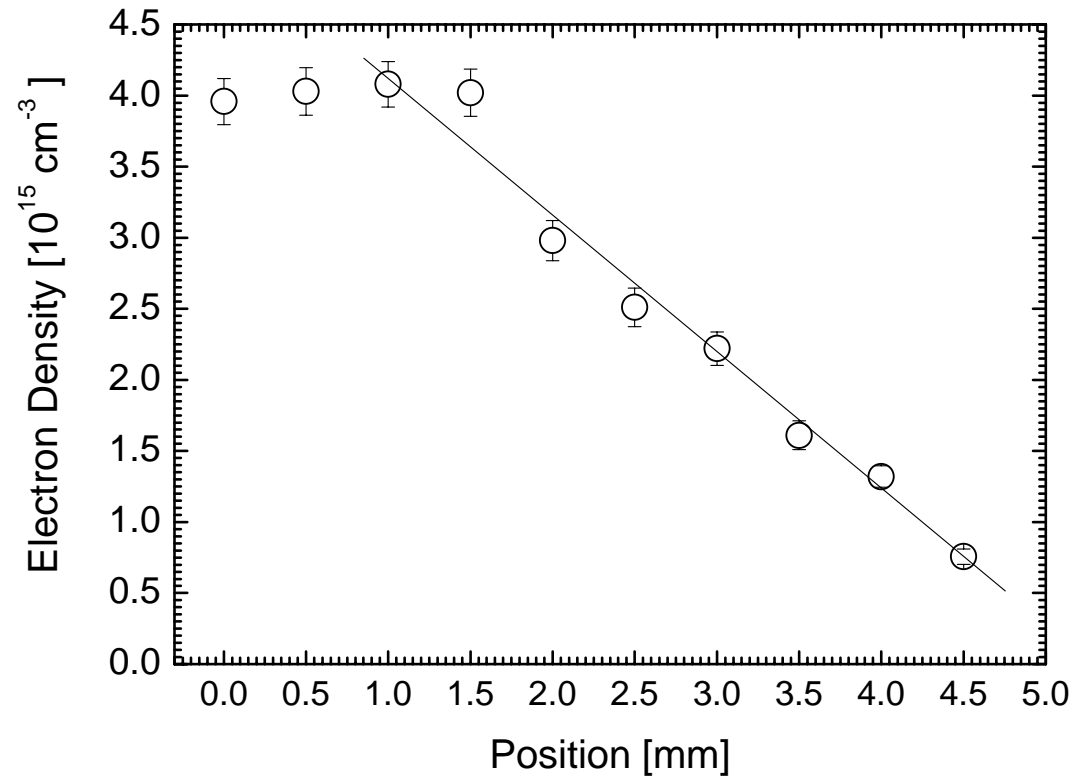


Figure 8.,

Spatial variation of the electron density at the discharge current of 50 A. We calculated the density from the Stark broadening width of He 667.8 nm, which is drawn from the deconvolution procedure of the experimental curve with a Voigt profile. For $x \geq 1.0$ mm, the density decreased linearly, as expected by the continuum flow model.

Figure 9, S. Namba et al., JJAP

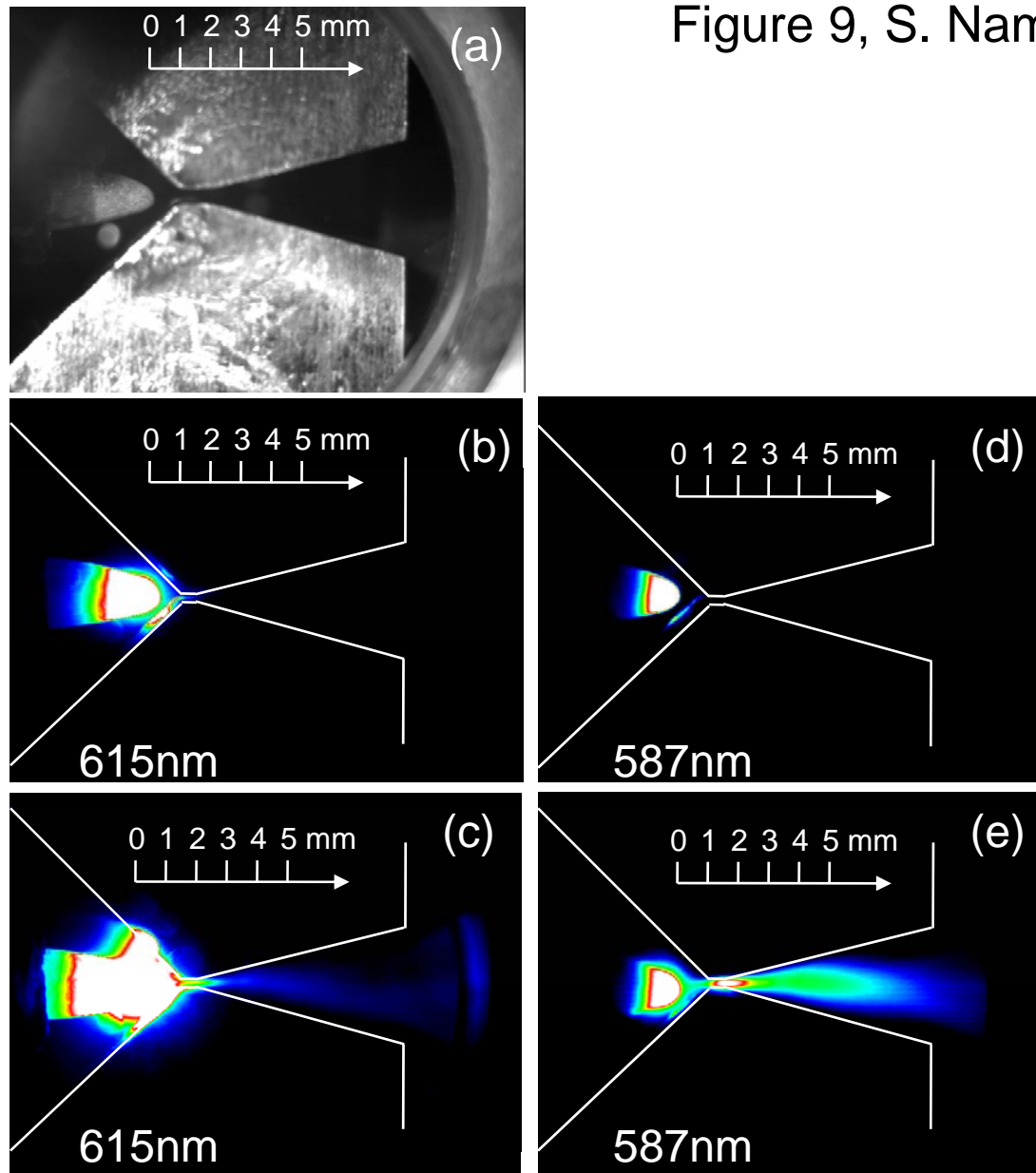


Figure 9.,

2D monochromatic emission images of plasma expansion taken by using the optical bandpass filters, 615 nm for (b) and (c), 587 nm for (d) and (e). As for (b) and (d), the thick ND filters were used for the appropriate light reduction.

Figure 10, S. Namba et al., JJAP

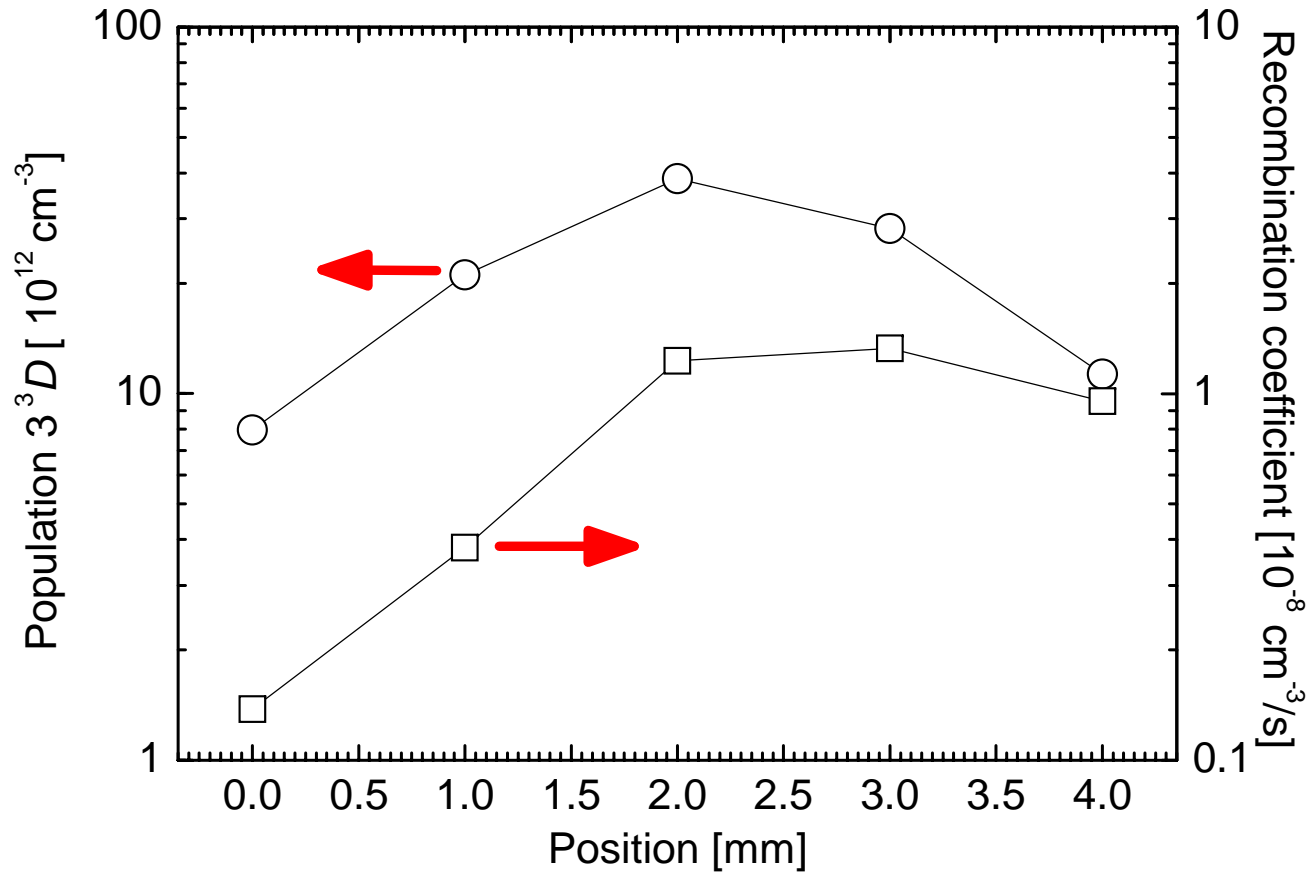


Figure 10.,
Population of $3d^3D$ level and the collisional-radiative recombination coefficient were calculated using the He collisional-radiative model.